

Purdue Physics REU conference
Agenda and Abstracts
August 1, 2024, room PHYS 242

- 9:00 Monique Morse. *Prospects of Top Quark Entanglement at the High Luminosity Large Hadron Collider (HL-LHC)*. (Dr. Jung)
- 9:20 Augustin Sanchez. *Precision measurement of the radial matrix elements for $6s \rightarrow 7p$ transitions in atomic cesium*. (Dr. Elliott)
- 9:40 Ana Colliton, Brian Borosky. *Response Dynamics in Acoustic Spectroscopy*. (Dr. Reppert)
- 10:10 Break
- 10:20 Adian Jacobsen. *A potential new measurement technique for the current phase relation of a topological insulator*. (Dr. Rokhinson)
- 10:40 Madison Whitmore. *Augmenting Fe-Triazolate Metal-Organic Framework (MOF) with Photosystem I*. (Dr. Pushkar)
- 11:00 Beny Verezub. *Laser Frequency Stabilization for the Purpose of Trapping Atoms on a Microring Resonator*. (Dr. Hung)
- 11:20 Joseph Carpenter. *Generating Multiply-Quantized Vortices in a Bose-Einstein Condensate with a Spiraling Potential Barrier* (Dr. Hung)
- 11:40 Lunch break (on your own)
- 1:00 Owen Gill. *Topological Phase of Graphene and Berry Curvature Computation*. (Dr. Varynen)
- 1:20 Lexy Hensley. *Machine Learning Analysis of Seismic Coda Signals to Monitor Shear and Hydraulic Stimulation in Fractured Rock at the Sanford Underground Research Facility*. (Dr. Pyrak-Nolte)
- 1:40 Erin Duell. *Examining Acoustic Wave Interactions with Fracture Intersections*. (Dr. Pyrak-Nolte)
- 2:00 Reagan Thompson. *Shearing Fracture Networks*. (Dr. Pyrak-Nolte)
- 2:20 The end
- 6:00 - *Farewell party/picnic at Sergei Savikhin's house for REU students*
Advisors & significant others are welcome, but please reply for count!
Address: 2505 McShay Dr., West Lafayette
Phone: 765-413-5026 (cell)

Prospects of Top Quark Entanglement at the High Luminosity Large Hadron Collider (HL-LHC)

Monique Morse^{1,2}, Isabella Freitas^{2,3}, Osama Dawood², Andreas Jung² (PI)

Saint Mary's College, IN | Purdue University, IN | Fermilab National Accelerator Laboratory, IL

This project investigates the prospects of quantum entanglement in top quark pair production at the high-luminosity large hadron collider (HL-LHC). High luminosity is a future update that will increase the instantaneous luminosity of the LHC beam to bring the center of mass energy from 13.6 TeV to 14 TeV. Beam improvements at the HL-LHC will yield about ~10x more data, multiplying the number of observable p-p collisions per bunch by a little over a factor of 4 [4]. To put this into perspective, the most recent run generated ~60 p-p interactions per bunch [4]. The HL-LHC is predicted to produce around ~250 [4]. This analysis aims to give a projection of the precision for entanglement measurements at the HL-LHC.

Particles are said to be entangled if their states cannot be described independently from one another [1]. They each carry information such that if you were aware of the behavior (spin) of one particle, you can deduce how the other behaves [1]. The CMS experiment is interested in top quark entanglement in particular because of its extremely short lifetime (5×10^{-25} s) [1]. Decaying before it can be hadronized by the strong force, the top quark makes for a rare instance in which entanglement effects can be examined at diminutive distances [2].

Due to the top quark's fast decay rate, its presence cannot be directly observed within the CMS detector [5]. Luckily, the top quark passes all of its spin information to its daughter particles (figure 3) [1]. Because of this, the entanglement observable D can be related to the normalized differential event cross-section as function of the angle between two leptonic decay products ($\cos\phi$) [1]. Entanglement is probed in the center of mass (CM) frame described by the helicity basis (figure 1), where the scattering angle (Θ) is sensitive to the spin correlations bounded by the top anti-top invariant mass ($M_{t\bar{t}}$) [1]. Quantum Chromodynamics (QCD theory) determines that D falls within a range of $-1 < D < -1/3$, and is calculated by the equations shown in figure 2 [1,2].

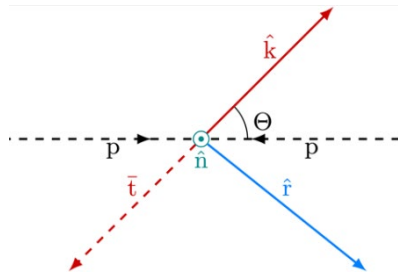


Figure 1: Diagram of helicity basis. Θ is the scattering angle, \hat{k} is the direction of the top quark product, \hat{p} is the proton beam(s), \hat{r} is the direction orthogonal to the top-antitop production axis, and \hat{n} is transverse with respect to the beam [1].

$$\cos \varphi = \hat{\ell}^+ \cdot \hat{\ell}^-$$

$$\frac{1}{\sigma} \frac{d\sigma}{d \cos \varphi} = \frac{1}{2} (1 - D \cos \varphi)$$

$$D = -\frac{\text{tr}[\mathbf{C}]}{3} = -(C_{kk} + C_{rr} + C_{nn})/3$$

Figure 2: The equations for D. The two ℓ 's in the first equation stand for the direction of the outgoing leptons. D is usually computed with the 2nd equation, where sigma refers to the event cross section. Very similar results can be produced with the third equation where C_{ij} are spin polarizations [1,2].

Since High Luminosity is a future phase, Monte-Carlo (MC) samples are generated to simulate top quark production. Selection cuts are then applied to these samples to ensure that the detector trigger properly chooses events relevant to our analysis [5]. The cuts are also in place to reduce background noise from low energy events outside of the analysis scope [4]. Additionally, event final states are limited to specific decay configurations (figure 3). After event selection, the analysis reconstructs the top quark from its daughter particles at the reconstruction level [5]. This allows the leptons to be boosted to the parent CM frame [5].

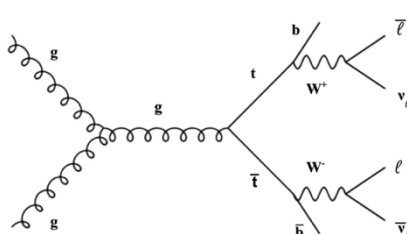
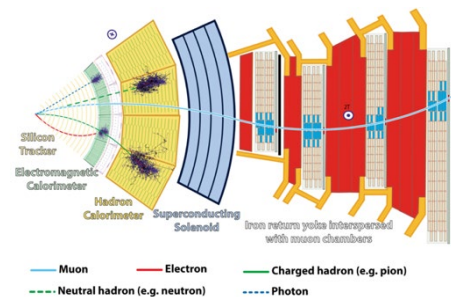


Figure 3: (left) Feynman Diagram for a dileptonic ($e^{+}/\mu^{+}/\tau^{+}/e^{-}/\mu^{-}/\tau^{-}$) final state. Configurations containing a b quark and lepton/neutrino pairs are chosen to facilitate the natural decay of top quarks formed from gluon-gluon interactions.

Figure 4: (right) Diagram of the CMS sub detectors for proton-proton collisions at the LHC. For more info see [7].



After the top quark is reconstructed, heat maps (such as the one in figure 5) are created. These depict an estimate of D at the generator level for lower $M_{t\bar{t}}$ masses (300–400 GeV range). Entanglement is not as obvious within the reconstructed simulation events as they have been ‘smeared’ by detector resolution, among other complications [4]. To return the results to the parton level and correct smearing from the detector, the samples were unfolded. Unfolding is a matrix inversion process that simulates the detector environment in order to bring the true, parton-level results forth from the reconstructed distributions [3]. For this analysis, 2D unfolding was performed using the response matrix given by the invariant mass ($M_{t\bar{t}}$) and the scattering angle (Θ). Following unfolding, D was recalculated with the corrected samples.

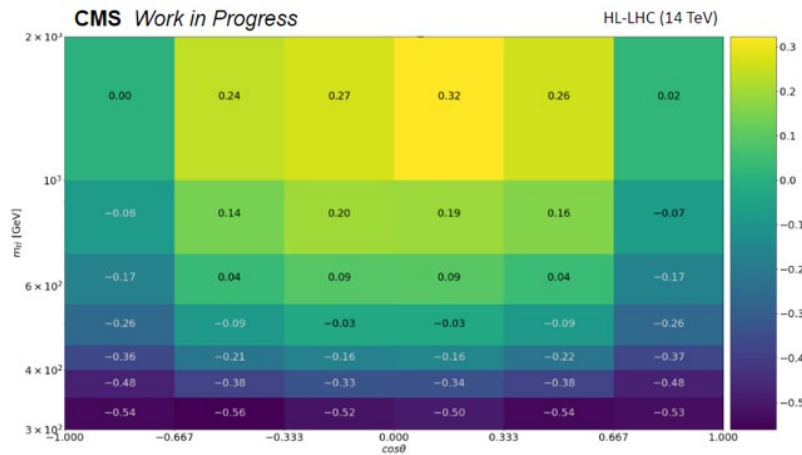


Figure 5: Heatmap of the entanglement observable D as a function of the ($M_{t\bar{t}}$) and ($\cos\Theta$) at the generator level within the parent CM frame.

The unfolded results (figure 6) support evidence for the possibility of entanglement at the HL-LHC within the lower $M_{t\bar{t}}$ region (300–400 GeV). Both the unfolded and generated predictions align with the theoretical entanglement patterns of top quarks produced by gluon-gluon fusion [2]. When the HL-LHC is up and running, these results will serve as a baseline from which entanglement can be measured. Any deviations from these estimates may prove to be governed by ‘new physics’ that exists beyond the standard model.

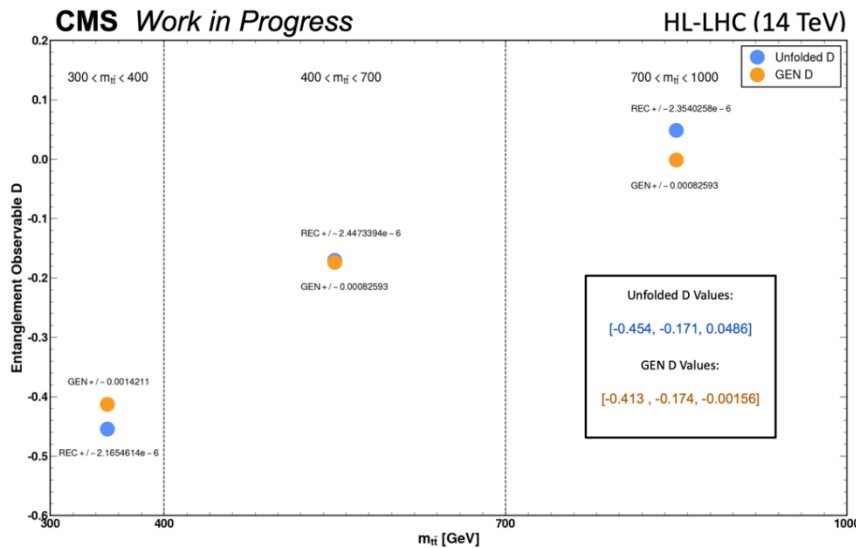


Figure 6: Future projection for nominal D values within the three $M_{t\bar{t}}$ ranges: 300–400, 400–700, 700–1000 GeV. Unfolded results are compared to the generator level. This plot doesn’t take any systematic uncertainties into account, just nominal ones.

The Jung CMS group is especially interested in this idea, which is why I have spent a large portion of the summer documenting every step of this analysis to pass on to future grad students that may work on this project with new MC samples.

With that, I would like to express my gratitude for all the wonderful people in the Jung group that have helped me this summer. I would first like to thank grad student Osama Dawood for his patience with Isabella and I during those long weekly lectures, and for not tiring of our endless questions. A special thanks to PhD student AJ Wildridge, your expert advice was crucial to my understanding of this project.

I would also like to thank Ling He and David Ruiter for their efforts to introduce me to the innerworkings and lingo of the Purdue CMS group at the beginning of the summer. To Isabella Freitas, my Fermilab partner, thank you for your contributions to this project and for your support over the past few weeks. Finally, I would like to thank my PI, Professor Andreas Jung for creating such a welcoming environment within the particle physics department. I was glad that I could always come to you with questions during the weekly meetings. I learned a lot from your explanations.

This work was supported by NSF REU grant PHY-224429.

References:

[1] <https://cds.cern.ch/record/2893854/files/TOP-23-001-pas.pdf>

+ corresponding internal CMS note

[2] <https://cds.cern.ch/record/2813262?ln=en>

+ corresponding internal CMS note

[3]

<https://indico.cern.ch/event/107747/contributions/32645/attachments/24317/35000/blobel.pdf>

[4] Conversation with AJ Wilderidge, July 24th, 2024

[5] Conversation(s) with Osama Dawood, June 2024

[6] <https://cms.cern/detector>

Precision measurement of the radial matrix elements for $6s \rightarrow 7p$ transitions in atomic cesium

Augustin Sanchez^{1,2}, D.S. Elliott²

¹Wabash College, Crawfordsville, IN, ²Purdue University, West Lafayette, IN

In quantum perturbation theory, matrix elements provide information about which atomic transitions are allowed and the strength of the transitions. The matrix elements of cesium are of particular interest due to their use in testing the strength of transitions induced by the parity non-conserving weak force [1]. This project focused primarily on performing high precision measurements following the procedure of previous work done by this lab [2] of the $6s^2S_{1/2} \rightarrow 7p^2P_{3/2}$ and $6s^2S_{1/2} \rightarrow 7p^2P_{1/2}$ transitions by direct comparisons of absorption spectra with the well-studied and precisely known $6s^2S_{1/2} \rightarrow 6p^2P_{1/2}$ transition [3].

To make a precise measurement of a matrix element using the absorption spectra would require precise knowledge of difficult to control variables of the experimental apparatus, the length of the cesium cell and the atomic vapor density of the cesium in the cell [2,4]. Instead, by measuring the absorption of a transition with a well-known matrix element and then rapidly switching to the transition of interest and comparing the ratios of the absorption strengths, the need to precisely known and control the length of the cell and the vapor density is no longer needed, so long as the measurements of the spectra are taken in rapid succession of one another. Figure 1 shows the energy level diagram of cesium and the transitions and references that are utilized for finding the ratios of the absorption spectra that can be used to find the matrix elements of interest.

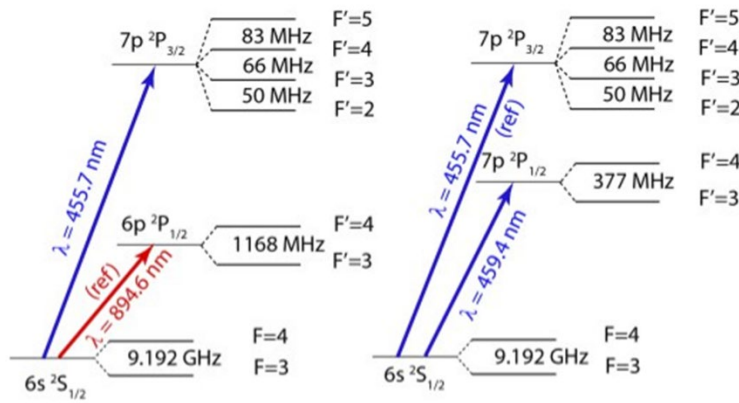


Figure 1: From [2] For the $6s^2S_{1/2} \rightarrow 7p^2P_{3/2}$ transition, the absorption ratio uses the $6s^2S_{1/2} \rightarrow 6p^2P_{1/2}$ transition. The $6s^2S_{1/2} \rightarrow 7p^2P_{3/2}$ is then used for the $6s^2S_{1/2} \rightarrow 7p^2P_{1/2}$ and not the $6s^2S_{1/2} \rightarrow 6p^2P_{1/2}$ since the strength of the $6s^2S_{1/2} \rightarrow 6p^2P_{1/2}$ transition is so much stronger than the $6s^2S_{1/2} \rightarrow 7p^2P_{1/2}$.

The experimental set-up is shown in Figure 2. This experiment utilized diode lasers in the Littrow configuration controlled by a piezo crystal and a laser-diode current feed-forward loop that allowed for the lasers to be scanned over the transitions without hopping modes. Currently, the frequency calibration is achieved by using two Fabry-Perot cavities, however in the future the frequency calibration will be performed by using a frequency comb, which will give more data points for the frequency calibration (~250 MHz spacing) than the current Fabry-Perot cavities (~1500 MHz spacing). The acousto-optic modulators are meant to stabilize the optical power going into the cell as the lasers scan. The hot cell is used to find

the amount of power in the edges of the laser's linewidth, and this is subtracted from the scans with the hot cell not present.

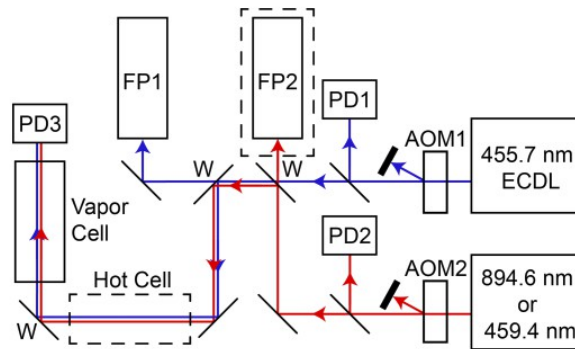


Figure 2: From [2] Experimental set-up FP- Fabry-Perot cavity, ECDL- external cavity diode laser (both in Litrow configuraton), PD- photodiode

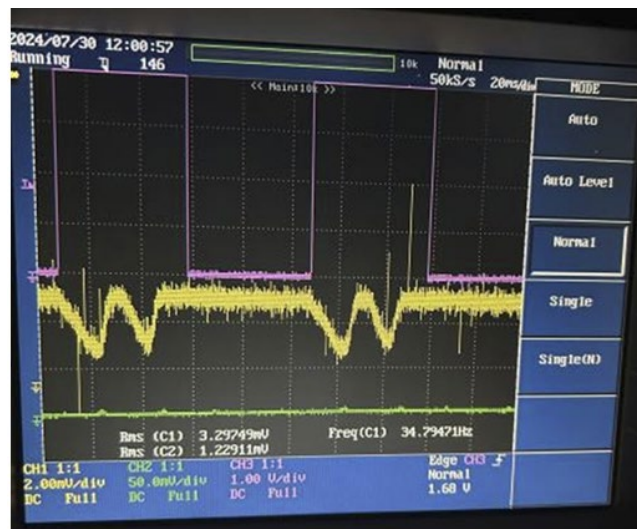


Figure 3: Image of scan from the 894 nm ($6s^2S_{1/2} \rightarrow 6p^2P_{1/2}$ transition) on an oscilloscope

This summer I worked on helping to set up this experiment and obtaining some preliminary data that has provided useful feedback to future experimental setup. I would like to thank Dr. Elliott for all his support and help throughout the summer and graduate students Jonah Quirk, Amy Damitz and Deigo Esteban who offered guidance and their support. This work was supported by NSF REU grant PHY-2244297.

References

- [1] S. A. Blundell, J. Sapirstein, and W. R. Johnson, Phys. Rev. D **45**, 1602

Response Dynamics in Acoustic Spectroscopy

Bryan Borosky^{1,3}, Ana G. Colliton^{2,3}, Mike Reppert³

¹ University of North Carolina at Chapel Hill, NC

² St. Olaf College, Northfield, MN

³ Purdue University, West Lafayette, IN

Infrared spectroscopy has proven to be instrumental in determining the behavior and structure of molecules, specifically within biological systems, due to the correlation between the structure of molecules and the absorption of resonant frequencies and vibrational modes of them. It was previously argued that the quantum nature of light harvesting was uniquely determined by the preservation of electronic coherence within the system¹. Conversely, recent work has also shown that the ‘quantumness’ of light harvesting is affected by the quantized nature of vibrational dynamics². Early experiments revealed that the anharmonic behavior of stringed instruments, such as guitars, can be analyzed using pump-probe-type measurements, providing an intuitive understanding of vibrational dynamics within an acoustic setting. These experiments offer a quantitative measure of acoustic anharmonicities, such as the "buzzing" from a poorly adjusted guitar string. The objective of this work is to create an acoustic analog to 2D infrared laser spectroscopy, similar to the aforementioned experiments, that probes the same kind of anharmonicities that arise within photosynthetic systems and allow for a greater intuitive understanding of the physical behaviors of such vibrational responses.

Vibrational response within acoustic instruments, like molecules, is governed by the framework of response theory. Within laser spectroscopy, response theory is embedded within the nature of electrodynamics, specifically as a perturbation framework within the electric susceptibility. Similar to a multipole expansion of an electric potential, certain terms of the perturbative series dominate in specific settings. In the presence of a low intensity perturbation, the linear response term of the series dominates and results in a simple response by the system. At higher intensity perturbations, however, the remaining terms of the series dominate and are understood to govern the system’s ‘nonlinear’ response. Numerical simulations have been utilized to better understand both classical and quantum responses within systems³ but suffer from the disadvantage that the nonlinear regime of response theory tends to diverge at large time scales⁴ and become unphysical. To combat this, we propose an analogous acoustic model, since observed response signals do not diverge in an experimental setting. Within our proposed acoustic analog to infrared spectroscopy, linear response can be understood as the simple response of a guitar string vibrating at a resonant frequency due to an incident perturbation. The nonlinear response of the system, however, would manifest as a shift in the response frequency due to the anharmonic nature of this response.

To measure both linear and nonlinear response in acoustic instruments, such as guitars, we designed an experiment that allows for the acoustic response of a guitar to be measured and controlled. Firstly, the guitar must be isolated from any sort of outside audio

disturbance, which can be accomplished by placing the guitar in a box lined with acoustic foam. This design acts as a barrier to any outside disturbance while also terminating the propagation and reflection of sound waves within the box. Secondly, the intensity of the perturbation experienced by the strings of the guitar must be controlled. This is most effectively accomplished by exploiting sound resonance. By exciting the guitar strings with a resonant sound pulse, we can control the intensity of the perturbation by adjusting the amplitude (or volume) of the pulse. The pulse utilized in this work was generated by convolving a gaussian curve with a cosine function to enable quick decay. This sound pulse can be subtracted from the final spectrum

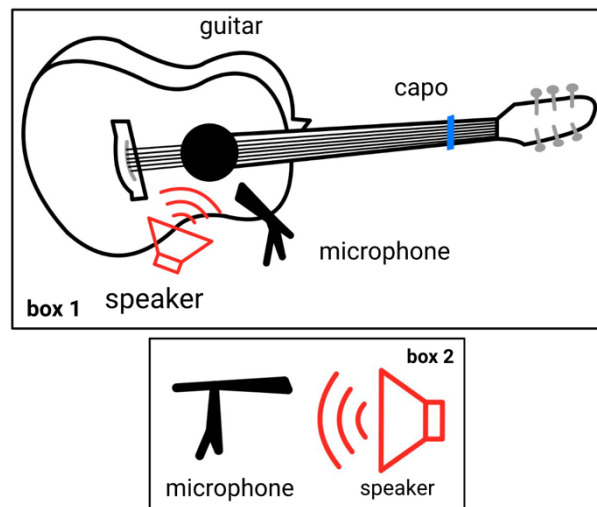


Figure 1 The experimental setup for data collection in this work, consisting of two acoustically isolated boxes with microphones and speakers. By including a second box without a guitar, the incident pulse can be subtracted from the final spectrum'

to accurately capture the response of the strings, which is accomplished by the use of a 'transfer function' analysis, a standard practice within the audio industry. The most effective way to construct this transfer function is to create a second audio channel, consisting of another microphone and speaker in a separate, acoustically isolated box. From there, the

sound pulse can be subtracted from the response. Naturally, this subtraction does not account for the effects of the resonance of the guitar body, which introduces a phase shift before subtracting the pulse. Thirdly, because musical instruments are designed to be harmonic in nature, it is necessary to modify the guitar to allow for the nonlinear response to dominate. Our modifications involved the design and construction of a specialized capo for the instrument, which included adjustable screws that allowed for the string vibrations to be damped, creating an effect analogous to 'fret buzz' produced by an instrument with poor action. These screws, in tandem with the controllable audio pulse, allows for a linear response to occur at low intensities and a nonlinear response to occur at

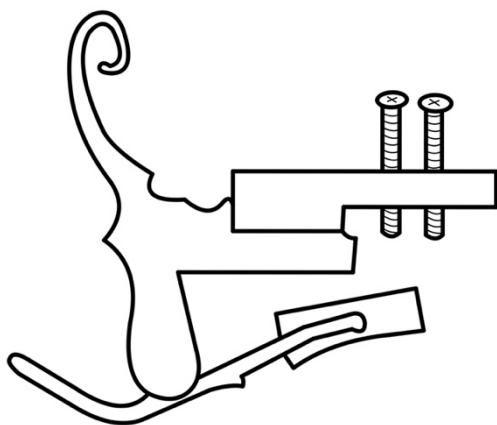


Figure 2 The schematic design for the modified capo used to promote anharmonicity from the guitar. Two screws sit close to the guitar strings to produce a nonlinear 'buzz' effect.

high intensities, replicating the axioms of response theory to some extent.

Using the aforementioned experimental design, we captured both the linear and nonlinear regimes of the theory within the responses of our instrument. To collect and process data, we wrote and utilized a Python script that enabled us to simultaneously play an audio pulse while also recording the response from the guitar. We first measured the response from

the strings without any nonlinear effects by simply playing an audio pulse at 75% volume into the guitar with damped strings and without damped strings. As expected, invoking the anharmonicity in the guitar caused a shift in the response frequencies of the strings.

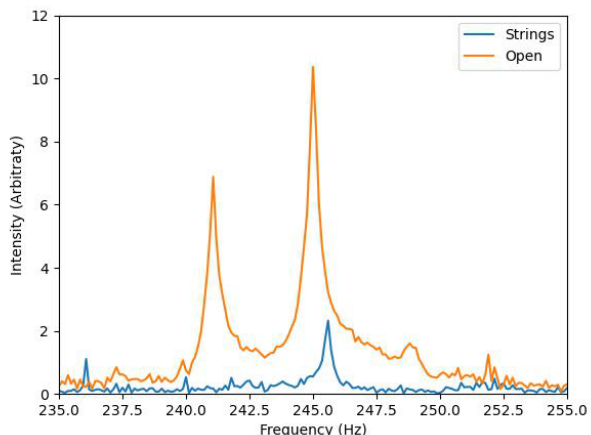


Figure 3 Spectra for two linear responses without damping (orange) and with damping (blue) from two resonant guitar strings. An obvious frequency shift occurs upon damping the strings, although this is still linear in nature

These results are displayed in Figure 3. The two peaks within the undamped spectrum correspond to the response of two closely tuned guitar strings. The response within the damped spectrum corresponds to the response from only one string since the lower frequency string was erroneously over-damped during data collection. Next, we probed how the nonlinear response behaves as a function of perturbation intensity by recording the response of the

guitar when subjected to a pulse at 75% volume and 50% volume. These two percentages were chosen for two reasons; firstly, a pulse of maximum volume would saturate the microphone recordings and negatively affect the phasing of the pulses, and secondly, a response below 50% volume would excite the strings too little and result in a purely linear spectrum. These results are pictured in Figure 4. This spectrum is more characteristic of an infrared spectroscopy absorption spectrum, purely for conventional sake. A clear relationship between perturbation intensity and the shift in response frequency can be seen upon comparing the two spectra, but further measurements with greater precision will be necessary to definitively determine the behavior of this relationship. There is an obvious phase twist within the spectrum, which we suspect was caused by resonance within the guitar body, indicating that a more effective data processing or experimental design will be necessary going forward.

While these measurements alone are not sufficient to construct a general understanding of response theory within acoustic terms, they do, at minimum, demonstrate that a greater understanding of it is feasible through similar means. We also found a somewhat unexpected necessity in our experimental design with respect to the placement of our measurement microphones. When oriented to face towards the measurement microphone, without the presence of the guitar, strange structure was observed in the Fourier transformed pulses. When both microphones were pointed away from the microphones, however, this

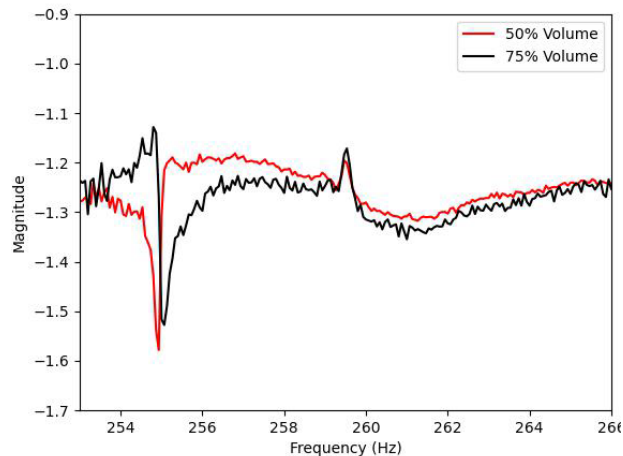


Figure 4 Spectra for two nonlinear responses at 50% volume (red) and 75% volume (black). A basic relationship between frequency shift and the intensity of the perturbation can be discerned. A 'phase twist' is evident within the spectrum by the lack of 'flatness' in the baseline.

structure vanished and the pulses appeared perfectly gaussian in nature, as we expected initially. We are unsure of what may cause the structure, but for further experimental purposes, we advise pointing the microphones away from the audio speakers. Through our efforts, we believe that we have created a solid foundation for the project should anyone desire to continue this work, potentially at a graduate-level. We would like to thank the Department of Physics and Astronomy at Purdue for inviting us to participate in the 2024 Purdue Physics REU Fellowship. We would also like to thank the Purdue Department of Chemistry for accommodating us during the summer. Lastly, we would like to thank Dr. Reppert and the Reppert group at Purdue for their support and for welcoming us into their group for the summer. This work was supported by NSF REU grant PHY-2244297.

References

- ¹ Jianshu Cao *et al.*; “Quantum biology revisited”. *Sci. Adv.* **6**, eaaz4888 (2020).
- ² Reppert, Mike; Brumer, Paul; "Quantumness in light harvesting is determined by vibrational dynamics". *J. Chem. Phys.*, 149, 234102 (2018).
- ³ Reppert, Mike; Brumer, Paul; “Classical coherent two-dimensional vibrational spectroscopy”. *J. Chem. Phys.* 14 February 2018; 148 (6): 064101
- ⁴ M. Kryvohuz and J. Cao, *Phys. Rev. Lett.* 96, 030403 (2006)

A potential new measurement technique for the current phase relation of a topological insulator

Aidan Jacobsen¹, Leonid Rokhinson¹

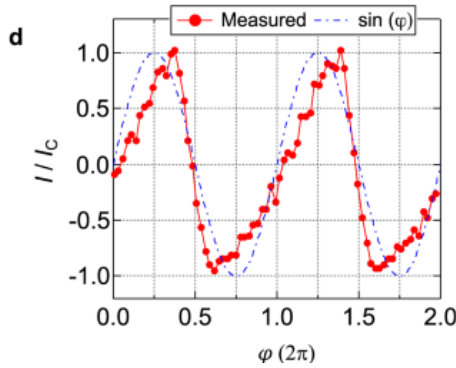
¹Purdue University, IN

Topological insulators are a class of material that has been proposed to host exotic quasiparticles such as Majorana Zero Modes. These quasiparticles have applications to topological quantum computing if braiding and fusion operations could be performed on a 2D surface, and to excite these quasiparticles, the topological insulator must be proximitized with superconductivity through a nearby superconductor^[1]. To show that a topological insulator is properly proximitized, various predictions of the model can be tested. One such property that can be measured is the current phase relation of a superconductor-topological insulator-superconductor (SC-TI-SC) junction.

For the typical SC-Insulator-SC junction, experiments have confirmed predictions that the current phase relation is given by one of Josephson's equations^[2]:

$$I_s = I_c \sin(\Delta\phi)$$

On the other hand, for a SC-TI-SC, non-sinusoidal current phase (CPR) relations are predicted^[3]. This measurement was performed on a junction of this type in 2020 using BiSbTeSe₂ as the topological insulator and superconducting Nb electrodes using an asymmetric SQUID^[4]. See below for the measured CPR from Morteza et al. Here, I propose a different method to measure the same physical quantity and report on my analysis progress so far.

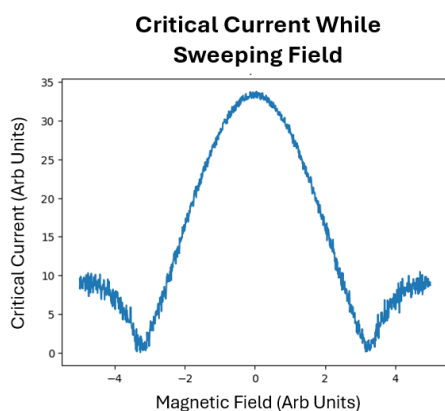
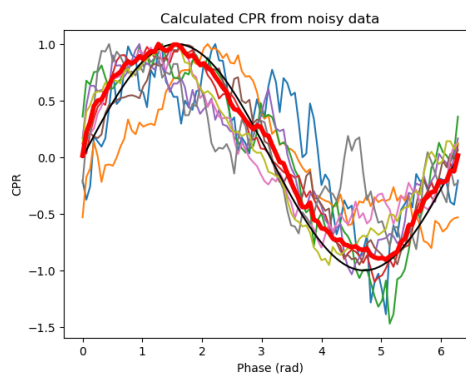


Since the critical current of a junction with finite width is given by the following integral, it can be difficult to directly extract because the current depends both on the distribution of current and the current phase relation. Here, γ is a parameter that is chosen so as to maximize I_c .

$$I_c = \text{Max} \left(\int_{-L}^L j_c(x) \text{CPR}(\gamma + \Delta\phi) dx \right)$$

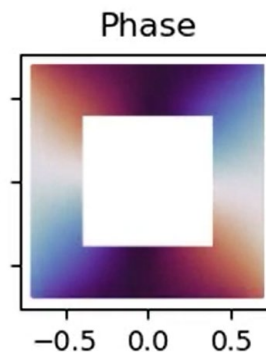
However, since the gauge invariant phase of a junction can be simulated, the CPR of a junction can be extracted from the critical current when I_c is measured at a variety of field strengths. By assuming a smooth CPR and current distribution, ϕ and x can both be discretized. This causes the integrand to only take on discrete values and changes the integration to a summation. The value of the integrand at each phase and x value can then be calculated. By plotting the integrand as a function of phase at a discrete x value, a trace of the CPR can be generated.

To validate the numerical methods, I constructed simulated data for a simple Josephson junction with some added noise. I then applied my method with $\gamma = \frac{\pi}{2}$, a known fact for the traditional Josephson junction, and reconstructed the CPR. The colored traces are individual measurements of the CPR, the red trace is the arithmetic average, and the solid black line represents the true CPR for this simulation. As can be seen from the closely matching average, this method has potential to extract CPR from this type of



data. Furthermore, I have developed an analysis technique to allow for γ to vary with the applied field to enable measurements of non-sinusoidal CPRs as well without strongly perturbing the measured CPR.

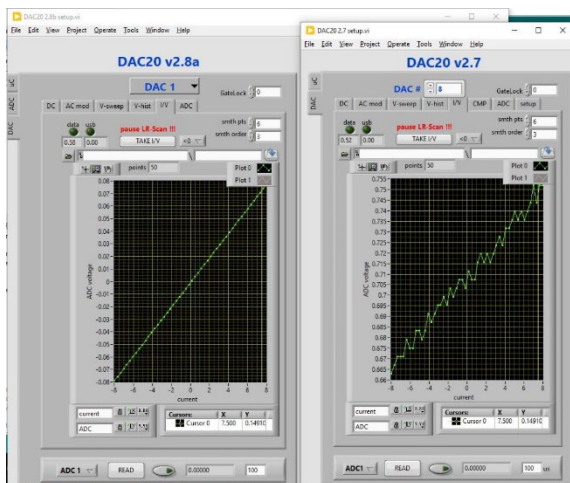
The second important part of this process is to be able to extract the phase across the width of the junction. I accomplished this using a Time Dependent Ginzburg Landau simulator^[5] for each side of the junction. A sample result of a simulation is shown below.



will extract the gauge invariant phases.

In order to reduce the noise on these measurements of critical current to an acceptable level, I have also been upgrading our lab's analog-to-digital converter. A sample current-voltage trace of a resistor can be seen below comparing the current system with the new system. A low noise level is critical to our measurement of CPR because the non-sinusoidal terms in CPR are easily washed out by excessive measurement noise. If using this method to extract the CPR of Josephson junctions is precise enough, it could be used as a

substitute for the standard methods because of the simpler nature of the device that needs to be fabricated.



I would like to thank Prof. Rokhinson and Prof. Vayrynen for the many insightful conversations and explanations that I have had with them over the course of this project. I would also like to thank Mingi Kim, Tai-Lung Wu, Jian Liao, Nemanja Ninkovic, and Hao Li for helping me learn about superconductivity this summer. This work was supported by NSF REU grant PHY-2244297.

Works Cited

[1]Fu, Liang, and C. L. Kane. “Superconducting Proximity Effect and Majorana Fermions at the Surface of a Topological Insulator.” *Physical Review Letters*, vol. 100, no. 9, 6 Mar. 2008, <https://doi.org/10.1103/physrevlett.100.096407>.

[2]Tinkham, Michael. *Introduction to Superconductivity*. Courier Corporation, 1996.

[3]Golubov, A. A., et al. “The Current-Phase Relation in Josephson Junctions.” *Reviews of Modern Physics*, vol. 76, no. 2, 26 Apr. 2004, pp. 411–469, <https://doi.org/10.1103/revmodphys.76.411>. Accessed 18 Apr. 2023.

[4]Kayyalha, Morteza, et al. “Highly Skewed Current–Phase Relation in Superconductor–Topological Insulator–Superconductor Josephson Junctions.” *Npj Quantum Materials*, vol. 5, no. 1, 30 Jan. 2020, <https://doi.org/10.1038/s41535-020-0209-5>. Accessed 19 Apr. 2020.

[5]Logan Bishop-Van Horn. “PyTDGL: Time-Dependent Ginzburg-Landau in Python.” *Computer Physics Communications*, vol. 291, 1 Oct. 2023, pp. 108799–108799, <https://doi.org/10.1016/j.cpc.2023.108799>.

Augmenting Fe-Triazolate Metal-Organic Framework (MOF) with Photosystem I

Madison Whitmore¹, Yulia Pushkar²

¹Smith College, MA, ²Purdue University, IN

Taking inspiration from the natural photosynthesis, artificial photosynthesis offers an attractive route to generate new fuel and energy sources. One desirable product is hydrogen gas, a possible alternative to fossil fuels. H₂ evolution through water oxidation has the potential to be more energy-efficient than current methods of H₂ production [1].

Approaches to artificial photosynthesis include producing purely artificial photoactive metal-organic frameworks (MOFs)[2], augmenting living systems with semiconductor nanocrystals[3], and combining the two. The latter involves isolating specific proteins involved in the process of photosynthesis and integrating those into the MOF or substituting other proteins for metal catalysts [4].

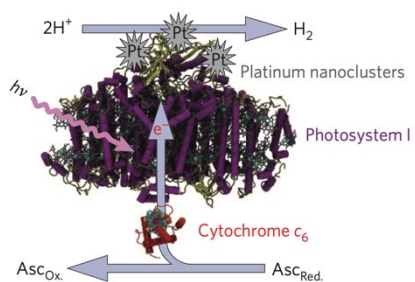


Figure 1 diagram of platinized PSI [4]

Photosystem I (PSI) is a protein responsible for transporting electrons from one side of the thylakoid membrane to the other, where the electron is passed to another protein to produce hydrogen. In a cell-free environment with a source of electrons and protons, PSI will still function provided it has a catalyst[4]. In the case of this research, photosystem I from the cyanobacterium *Synechocystis* sp. PCC 6803[5] was shown to evolve hydrogen when supplied with 0.1 mM PtCl₆ and 20 mM sodium ascorbate to act as a sacrificial electron donor. This platinized PSI (Figure 1) had an initial H₂ evolution rate of ~ 0.02 μmol H₂ (mg chlorophyll h⁻¹) which is comparable with the literature[4] considering the use of a less-optimized system of hydrogen detection and lower chlorophyll concentration.

A Fe-triazolate [Fe(ta)₂] metal-organic framework (MOF) was employed for H₂ evolution due to its photocatalytic activity and made up of earth-abundant metal. It has been shown to function similarly to the photosystem II protein in that it can oxidized water into oxygen gas and protons, which are used as the source for H₂ evolution. Due to the porous nature of MOFs, PSI was inserted into the gaps of Fe(ta)₂ by stirring Fe(ta)₂ in the aqueous PSI solution previously described. The solution was then centrifuged to separate the aqueous and PSI-incorporated Fe(ta)₂ (PSI@Fe(ta)₂) components and the UV-vis absorptions of the aqueous solution before and after stirring were compared to ascertain the amount of PSI incorporation. The sodium ascorbate was then washed away and the Fe(ta)₂ and PSI were resuspended in a 20 mM MES buffer and PtCl₆ was added to the final concentration of 0.1 mM. With no source for electrons besides those produced by water oxidation performed by Fe(ta)₂, the PSI functions as an

Photosystem I (PSI) is a protein responsible for transporting electrons from one side of the thylakoid membrane to the other, where the electron is passed to another protein to produce hydrogen. In a cell-free environment with a source of electrons and protons, PSI will still function provided it has a catalyst[4]. In the case of this research, photosystem I from the cyanobacterium *Synechocystis* sp. PCC 6803[5] was shown to evolve hydrogen when supplied with 0.1 mM PtCl₆ and 20 mM sodium ascorbate to act as a sacrificial electron donor. This platinized PSI (Figure 1) had an initial H₂ evolution rate of ~ 0.02 μmol H₂ (mg chlorophyll h⁻¹) which is comparable with the literature[4] considering the use of a less-optimized system of hydrogen detection and lower chlorophyll concentration.

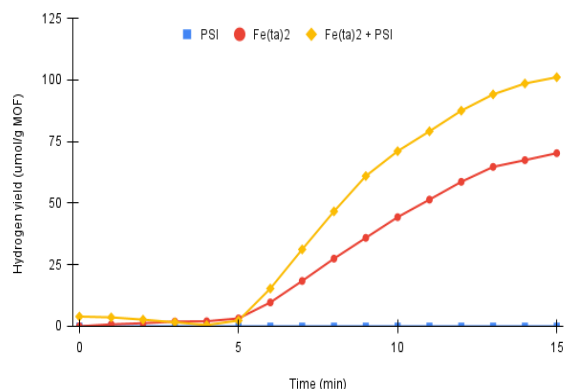


Figure 2 H₂ evolution results, all samples platinized

additional antenna for photon absorption. The result of this preparation is a MOF-bioprotein hybrid system that produced a greater H₂ yield than the MOF or PSI alone (Figure 2).

With a means of improving the photocatalytic H₂ evolution of MOFs, the next step of this research would be testing the process with other MOFs such as those previously investigated by the Pushkar group[6].

I would like to thank Dr. Pushkar for answering the questions I had, as well as Dr. Patel for her guidance and patience in matters of chemistry. Additionally, I thank Sebastian Aguiar Castrillon for the introduction to vibrational spectroscopy unrelated to this project. This work was supported by NSF REU grant PHY-2244297.

References:

1. <https://www.eia.gov/energyexplained/hydrogen/production-of-hydrogen.php#:~:text=The%20two%20most%20common%20methods,hydrogen%20production%20methods%2C%20or%20pathways>
2. C. Yavuz & S. Erten-Ela. “Solar light-responsive α -Fe₂O₃/CdS/g-C₃N₄ ternary photocatalyst for photocatalytic hydrogen production and photodegradation of methylene blue”. *Journal of Alloys and Compounds*, 2021. <https://doi.org/10.1016/j.jallcom.2022.164584>.
3. E. Edwards et al. “*Shewanella oneidensis* MR-1 respire CdSe quantum dots for photocatalytic hydrogen evolution”. *PNAS*, 2023. <https://doi.org/10.1073/pnas.2206975120>.
4. I. Iwuchukwu et al. “Self-organized photosynthetic nanoparticle for cell-free hydrogen production”. *Nature Nanotechnology*, 2009. DOI: 10.1038/NNANO.2009.315.
5. S. Savikhin et al. “Ultrafast Primary Processes in Photosystem I of the Cyanobacterium *Synechocystis* sp. PCC 6803”. *Biophysics Journal*, 1999. [https://doi.org/10.1016/S0006-3495\(99\)77480-1](https://doi.org/10.1016/S0006-3495(99)77480-1).
6. J. Patel et al. “Rational Design of Improved Ru Containing Fe-Based Metal-Organic Framework (MOF) Photoanode for Artificial Photosynthesis”. *Small*, 2024. DOI: 10.1002/sml.202310106

Laser Frequency Stabilization for the Purpose of Trapping Atoms on a Microring Resonator

Beny Verezub^{1,2}, Chen-Lung Hung²

¹ Lake Forest College, ²Purdue University

A microring resonator is a circular waveguide only tens of micrometers across. Inside, light can be trapped and will resonate at certain frequencies as with a traditional optical cavity. The microring is thermally locked to resonate at the atomic transition frequency of the master laser. However, to create a trap for the atoms, more light is needed in the ring: red detuned light to attract and blue detuned light to repel [1]. We use the master laser to stabilize the frequency of the two slave lasers. These slave lasers can be tuned in real time, and locked, to the resonant frequency through a feedback system based on the error signal of each individual laser [2]. When the atoms are trapped, you can interact with them using light. Depending on the state of the atom trapped, light of a frequency may be absorbed or transmitted down the bus waveguide.

My work revolved around locking the slave lasers to the master laser. The setup has three major parts: a scanning cavity, an Arduino microcontroller, and a function generator. The Arduino triggers the function generator to send a ramp signal to the scanning cavity. The master and the slave lasers pass through this scanning cavity when the cavity length reaches the resonant condition. The Arduino will capture the time of the resonant transmission. Using the ratio of master-to-master resonant time and master-to-slave resonant time, an error signal is obtained. The Arduino then sends a feedback signal to the piezos controlling the slave lasers to tune their frequency such that the error signal is minimized. Essentially, a PID controller attempts to tune the lasers in real time so that they can continuously resonate with the microring, keeping the trap active.

I would like to thank Purdue University for the opportunity to do research as well as Professor Chen-Lung Hung for welcoming me into his lab for this project. I

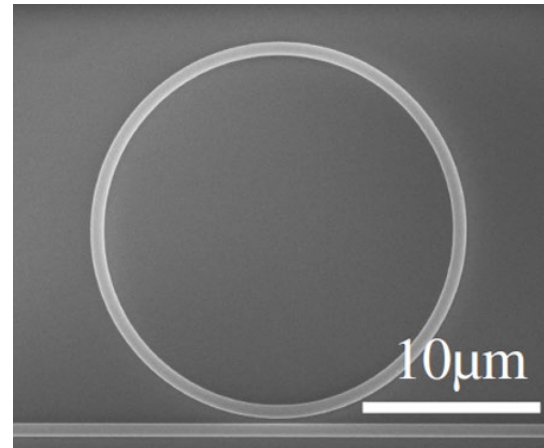


Figure 1: A microring waveguide and a bus waveguide beneath it [1].

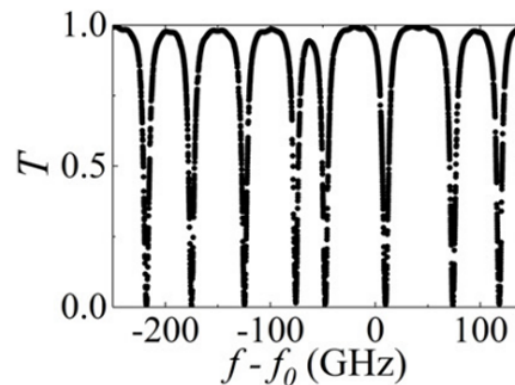


Figure 2: Transmission vs Frequency of the bus waveguide. At different resonances, the light goes into the microring and so the bus sees no light [3].

would also like to thank Dipanjan Das and Xinchao Zhou for helping with the work and answering questions. This project was funded by NSF REU grant PHY-2244297.

References:

1. T-H. Chang, B. M. Fields, May. E. Kim, and C-L. Hung, *Optica* **1203**, (2019).
2. S. Subhankar, A. Restelli, Y. Wang, S. L. Rolston, and J. V. Porto, *Review of Scientific Instruments* **90**, (2019).
3. T-H. Chang, X. Zhou, M. Zhu, B. M. Fields, and C-L. Hung, *Applied Physics Letters* **117**, (2020).
4. X. Zhou, H. Tamura, T-H. Chang, and C-L. Hung, *Physical Review X* **14**, (2024).

Generating Multiply-Quantized Vortices in a Bose-Einstein Condensate with a Spiraling Potential Barrier

Joseph Carpenter^{1,2}, Sambit Banerjee², Chen-Lung Hung²

¹Lawrence University, WI, ²Purdue University, IN

One of the characteristics of a superfluid is the quantization of vortices which flow indefinitely around a point of zero density. Certain Bose-Einstein condensates, which are systems of bosons which all share the same quantum state, have been observed to behave as superfluids, and have exhibited quantized vortices. These vortices provide insight to the behavior of quantum systems - such as their emergence from quantum turbulence [1] or their similarities with the ergoregion of black holes [2]. To facilitate the study of these vortices, it is important to discover replicable methods of generating vortices, with control over their number, location, direction, and quantization.

We drew upon the method outlined in Wilson et al. to establish a method of generating a central multiply-quantized vortex in our system [3]. The method involves spiraling a potential barrier created by blue-detuned light into the center of a 2D condensate. The blue-detuned light repulses atoms and causes flow around the potential barrier it creates.

We used an optical trap to create a 2D Bose-Einstein condensate of cesium-133 with a radius of 21 μ m. We used a blue-detuned laser to create a moving potential barrier. A digital micromirror device (DMD) controlled the location of the potential barrier. We used Python to create true-false frames for the DMD to trace the spiral pattern with adjustable parameters. Images of the condensate were taken using time-of-flight and in situ imaging and allowed us to determine whether a vortex was multiply quantized [4].

Much of my work was focused on programming the DMD to generate the desired spiraling potential barrier. We developed code to command the DMD to create the spiraling shape described, as well as several other methods involving the use of “chopsticks” to create pairs of singly quantized vortices [5]. We also worked on writing code to communicate to a function generator which we used to generate a square wave trigger input to the DMD, establishing the frame rate.

We adjusted the parameters of the spiral from Wilson et al. to fit our system. Our first trial produced many singly-quantized vortices, but no clear evidence of a multiply-quantized vortex. We conducted the experiment again with readjusted parameters and were able to observe the consistent formation of a multiply-quantized vortex.

I would like to express my gratitude to Professor Chen-Lung Hung for the guidance he has provided during my work, and to Sambit Banerjee for working with and supporting me during this project. This project was funded by NSF REU grant PHY-2244297.

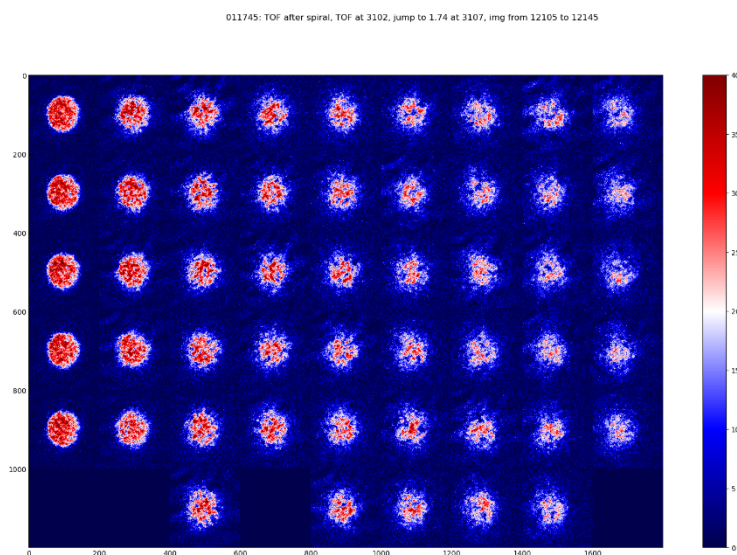


Figure 5 - Time-of-flight results from the first trial showing evidence of many singly-quantized vortices

References

1. Johnstone, et al. "Evolution of large-scale flow from turbulence in a two-dimensional superfluid", *Science* **364** 2019.
<https://doi.org/10.1126/science.aat57>
2. Giacomelli, Luca and Carusotto, Iacopo. "Ergoregion instabilities in rotating two-dimensional Bose Einstein condensates: Perspectives on the stability of quantized vortices", *Phys. Rev. Research* **2**, 2020.
<https://doi.org/10.1103/PhysRevResearch.2.033139>
3. Wilson, et al. "Generation of high-winding-number superfluid circulation in Bose-Einstein condensates", *Physical Review A* **106** 2022. <https://doi.org/10.1103/PhysRevA.106.033319>
4. Wright, et al. "Driving Phase Slips in a Superfluid Atom Circuit with a Rotating Weak Link", *Physical Review Letters* **110** 2013.
<https://doi.org/10.1103/PhysRevLett.110.025302>
5. Banerjee, et al. "Collapse of a quantum vortex in an attractive two-dimensional Bose gas".

Topological Phase of Graphene and Berry Curvature Computation

Owen Gill^{1,2}, Jukka Vayrynen²

¹Haverford College, ²Purdue University IN

Graphene is a unique material, exhibiting properties of Dirac fermions and a distinctive hexagonal lattice structure. In the realm of topological phases of matter, the work of condensed matter researchers such as Dr. Haldane laid the groundwork for the modern study of topological phases of matter, including Haldane's specific case the study of Chern insulators which exhibit the Quantum Anomalous Hall Effect [3]. My work this summer revolved around an introduction to the field of condensed matter research as a whole along with a specific focus on (i) utilizing the unique two-dimensional structure of graphene to transform the material into a topological phase of matter via the Haldane model, and (ii) inquiry into the underlying physics and mathematical structure underpinning this transformation and the ensuing topological properties.

Prior to arriving at Purdue for the summer REU program I had little to no experience modeling condensed matter systems. Under the guidance of Professor Jukka I. Vayrynen, I began my summer research project scripting models for simplified condensed matter systems hallmarked by nearest neighbor hopping's in one and two dimensions. This process required deriving Bloch Hamiltonians in both real and momentum space to describe the underlying physics of the subject system as well as using the eigen relation of the general time independent Schrodinger equation in addition to speculative Ansatz wave function solutions to parameterize the energy eigen values in a momentum basis. Once I was familiar with the process and method for modeling condensed matter systems, I went on to derive a model for a simple graphene lattice within the broader context of nearest neighbor and tight-binding models.

Considering two distinct sublattices of A site and B site points, the Hamiltonian I derived considers hopping terms between A and B sites along three (3) nearest neighbor vectors. [4]

$$H = \sum (a_j^\dagger b_{j+dn}) - \sum (b_j^\dagger a_{j-dn})$$

Expanding this Hamiltonian in momentum space by Fourier transformation of relevant operators into a momentum basis and simplifying complex terms, I was able to derive the simplified expression for the Hamiltonian in a momentum basis shown in [Figure 1](#). [4][5] From the energy bands of graphene plotted in momentum space (shown in [Figure 2](#)) several important observations relevant to the Haldane model can be made, including (i) that the lattice evidently contains two distinct Dirac points, (ii) where the energy bands display a linear dispersion relation, and (iii) that these Dirac points appear to be protected by both lattice symmetry (inversion symmetry) and time reversal symmetry. [2][4]

$$\begin{aligned} \delta_1 &= \frac{a}{2} \{1, \sqrt{3}\}; \\ \delta_2 &= \frac{a}{2} \{1, -\sqrt{3}\}; \\ \delta_3 &= -a \{1, 0\}; \\ k &= \{k_x, k_y\}; \\ \chi &= e^{i \cdot (k \cdot \delta_1)} + e^{i \cdot (k \cdot \delta_2)} + e^{i \cdot (k \cdot \delta_3)}; \\ \chi^* &= e^{-i \cdot (k \cdot \delta_1)} + e^{-i \cdot (k \cdot \delta_2)} + e^{-i \cdot (k \cdot \delta_3)}; \\ \mathcal{H}_{kb} &= \text{MatrixForm} \left[\begin{pmatrix} 0 & \chi \\ \chi^* & 0 \end{pmatrix} \right]; \end{aligned}$$

Figure 1. Illustrating the form of the Bloch Hamiltonian for traditional graphene structure.

version of the system may help.

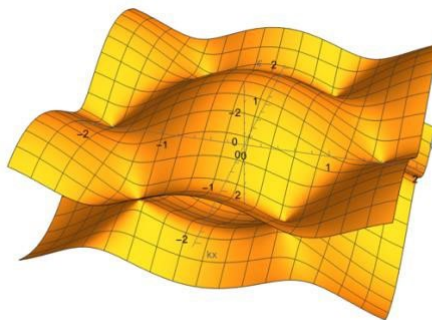


Figure 2. Illustrating the energy bands of traditional graphene, Dirac points are clearly visible along with the hexagonal lattice structure.

To transform this traditional phase of graphene into a topological one, I followed a process similar to that of Dr. Haldane in his original 1988 paper. To break inversion symmetry, oppositely signed-off diagonal mass terms ϵ and ϵ^* are introduced. This term alters the allowed quantum states on any pair of sites related by lattice spatial inversion – akin to raising the possible quantum states of one of the paired sites while lowering the other and thereby essentially breaking any inversion symmetry present. To break time reversal symmetry, a purely imaginary chiral second neighbor hopping term is introduced. Note that this term must propagate in opposite directions for A and B sites respectively to cancel any resulting induced magnetic flux term, intuitively breaking the symmetry of any time inversion operation while also preserving the anomalous hall effect. To introduce the mass terms, we can add ϵ and ϵ^* directly to the off-diagonal terms of the 2x2 Bloch Hamiltonian in the momentum basis as they have no strict momentum dependence. The second neighbor terms are more complicated involving consideration of second hopping terms between A and A sites and B and B sites along second neighbor vectors as well as an additional and arbitrary complex phase term to account for phase acquired in second hopping due to the Aharonov-Bohm effect. [2][3]

$$H_{\text{Haldane}} = t_2 i e^{i\phi} (\sum (a_j^\dagger a_{j+b}) - \sum (b_{j+b}^\dagger b_{j+d+b})) + \text{h.c.}$$

$$H_{\text{Mass}} = \epsilon \sum (a_j^\dagger b_{j+d}) - \sum (b_j^\dagger a_{j-d})$$

Once again expanding this Hamiltonian in real space by Fourier transformation of relevant operators into a momentum basis and simplifying complex terms I was able to derive the simplified expression for the Haldane term and mass term shown in [Figure 3](#). Combining these expressions, the complete Hamiltonian for the Haldane model can be derived. [1][2]

```

(* Cross Terms *)
i = t1*(e^(ikx*(ky)-delta1) + e^(ikx*(ky)-delta2) + e^(ikx*(ky)-delta3)) ;
j = t1*(e^(-ikx*(ky)-delta1) + e^(-ikx*(ky)-delta2) + e^(-ikx*(ky)-delta3)) ;

(* Diagonal Terms *)
l = 2*t2*Sin[phi]*(Sin[(kx, ky).b1]+Sin[(kx, ky).b2]+Sin[(kx, ky).b3]) ;
m = -2*t2*Sin[phi]*(Sin[(kx, ky).b1]-Sin[(kx, ky).b2]+Sin[(kx, ky).b3]) ;
n = 2*t2*Cos[phi]*(Cos[(kx, ky).b1]+ Cos[(kx, ky).b2]+ Cos[(kx, ky).b3]) ;

(* Populating Hamiltonian 2x2 Matrix *)
H11 = e + n + l ;
H12 = i ;
H21 = j ;
H22 = -e + n + m ;
H = MatrixForm[{{H11, H12},
                {H21, H22}}];

```

Figure 3. Illustrating the form of the Bloch Hamiltonian for The Haldane model of graphene with Haldane terms l, m, n and mass term epsilon

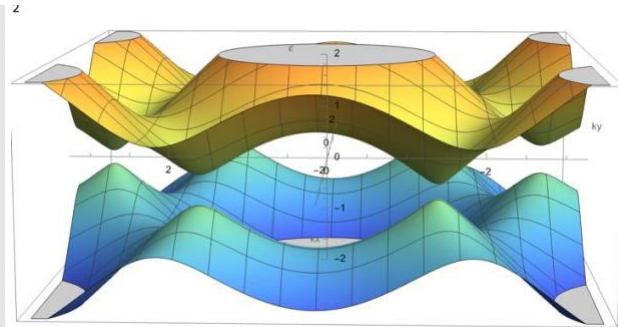


Figure 4. Illustrating the energy bands for the Haldane model of graphene, band gap and a and b sub lattice symmetry breaking are clearly visible.

From the plotted energy bands shown in [Figure 4](#), gapping of the positive band from the negative can be observed which corresponds to the breaking of inversion symmetry. Asymmetries in the structure of the energy bands can also be seen where they are symmetric across A sites and B sites but not between A sites and B sites which corresponds to breaking time reversal symmetries.

To explore the underlying topology of the Haldane model, it is necessary to examine the Berry curvature from which the topological invariant of the system, the Chern number, can be derived. As someone who is new to both condensed matter research and the mathematical field of topology, I found it helpful to derive for myself the geometric phase term originally identified in the quantum adiabatic theorem which is mathematically derived from the time-dependent Schrödinger equation. [6] The geometric phase, also known as the Berry phase after physicist Dr. Michael Berry, is acquired by the wave function as it traverses a closed loop in its parameter space and described by the global phase evolution of a complex vector as its parameters are adiabatically varied. [2] The Berry phase is given by the line integral of the Berry connection over a closed path in parameter space. [2]

$$\gamma(C) = \oint_C \mathbf{A}(k) \cdot d\mathbf{R} \gamma(k) = \oint_C \mathbf{A}(k) \cdot dk$$

Here, the Berry connection $\mathbf{A}(k)$ is a gauge field in momentum space. The curl of the Berry connection is the Berry curvature, $\mathbf{B}(k)$, which behaves like a pseudo-magnetic field in momentum space. [3]

$$\mathbf{B}(k) = \nabla \times \mathbf{A}(k)$$

An intuitive argument for the topological invariance of the system can be made from this standpoint. The gauge invariance of the Berry curvature implies that if the system remains topologically robust, the integral of the Berry curvature across the Brillouin zone should remain robust against local perturbations. This integral is precisely the Chern number. Thus, the gauge invariance of the Berry curvature leads to the topological robustness of the Chern number. Hence, the Chern number, as the integral of the Berry curvature across the Brillouin

zone, is a topological invariant, reflecting the global properties of the system's band structure.

In developing an algorithm to calculate the Chern number, I encountered an important consideration: the choice of gauge when plotting the Berry curvature. The Bloch wave function must be continuous across the entire Brillouin zone to ensure accurate calculation. This can be achieved by considering small plaquettes within the Brillouin zone in momentum space, ensuring that the Bloch functions are locally continuous within each plaquette. [2]

$$C = \frac{1}{2\pi} \int_{\text{BZ}} \mathbf{B}(\mathbf{R}) \cdot d^2\mathbf{R} = \frac{1}{2\pi} \sum \varphi_n \text{ where } \varphi_n = \oint \mathbf{A}_n(\mathbf{k}) \cdot d\mathbf{k}$$

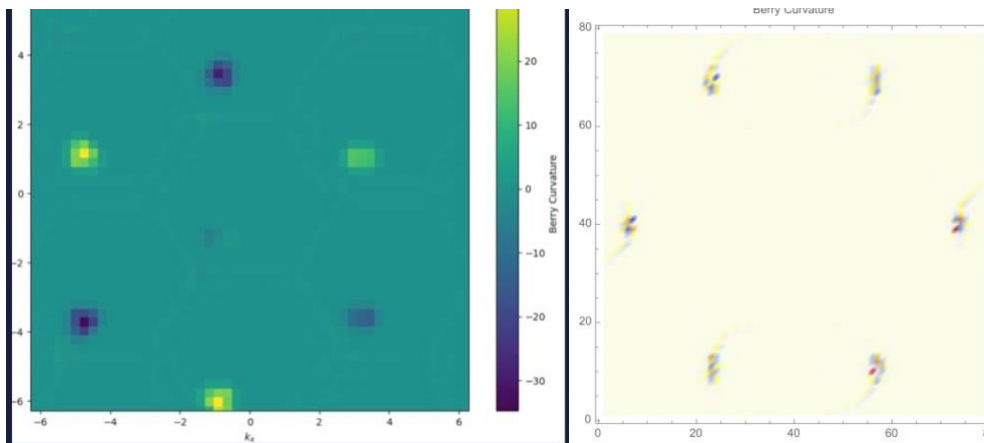


Figure 5. Work in progress plots of Berry Curvature for the Haldane model using my algorithm.

I would first like to thank Professor Väyrynen for all his guidance and support this summer in conjunction with my project. I would also like to thank Professor Savikhin for his efforts in organizing and running the REU program here at Purdue, as well as a fellow undergraduate research student Haixuan for his help in the beginning stages of my project. Finally, I would like to thank the NSF for their generous REU grant which funded this project. PHY-2244297".

References:

1. <https://phys-drp.mit.edu/sites/default/files/thaodinh.pdf>
2. <https://topocondmat.org/>
3. <https://www.youtube.com/@topologicalquantummatter-w4105>
4. https://www.weizmann.ac.il/condmat/oreg/sites/condmat.oreg/files/uploads/2015/tutorial_1.pdf
5. https://cpb-usw2.wpmucdn.com/u.osu.edu/dist/3/67057/files/2018/09/graphene_tightbinding_model-1ny95f1.pdf
6. <https://www.youtube.com/watch?v=pgEFvhkEp-c>

Machine Learning Analysis of Seismic Coda Signals to Monitor Shear and Hydraulic Stimulation in Fractured Rock at the Sanford Underground Research Facility

Alexis Hensley ¹, David D. Nolte ², and Laura Pyrak-Nolte ²

¹Berea College, KY, ²Department of Physics and Astronomy, Purdue University, IN

Geothermal energy production from the Earth's subsurface often relies on the flow of fluids through a network of fractures to extract heat. However, these fracture networks are sensitive to engineered and natural processes that open and close fractures in response to changes in stress, fluid pressures, and geochemical interactions. A challenge is linking information in geophysical data to changes in the network permeability to update numerical simulators to predict and control long-term energy production.

We use machine learning (ML) to explore data from Enhanced Geothermal Systems (EGS) Collab experiments at the Sanford Underground Research Facility (SURF) in Lead, South Dakota. Experiments at the 4100' level (see **Figure 1**) were monitored using a Continuous Active-Source Seismic Monitoring (CASSM) system. The SURF was once a gold mine and has since been repurposed to host a variety of experiments where a characterized underground setting is necessary.

The CASSM system was distributed around a known fracture within the testbed. The CASSM system used 20 3-channel accelerometer sources and 72 receivers to provide near-continuous observations from 2018 to 2022 during induced fracturing as well as shearing of known fractures. The full waveforms contained codas from multiple reflections from existing and induced fractures.



Figure 1. A Homestake Mine model with the conceptual designs of testbeds 1 and 2. Data for mine levels were from <http://homestake.sdsmt.edu/DXF/DXF.htm> (William Roggenthen, SDSMT). Testbed designs are from Joseph Morris of LLNL. The model was built and animated by Pengcheng Fu of LLNL.

We utilized a triplet loss neural network for signature identification of induced fractures during injection and pressurization tests. Essentially, the triplet loss neural network enables examination of the similarities and differences, by minimizing the distance between similar signals and maximizing the distance between dissimilar signals, as shown in **Figure 2**. Therefore, the neural network facilitates cross-examination of data from around the known fracture to look for localized fracture features within the similarities in signals from different source receiver pairs.

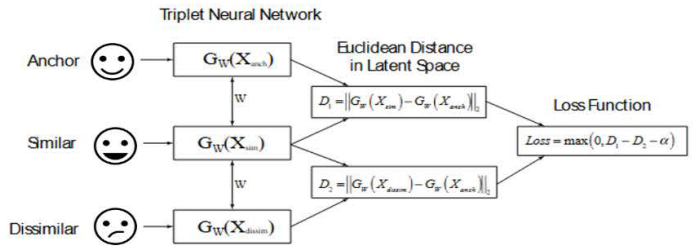


Figure 2. The triplet loss neural network.

This fracture yielded a temperature anomaly and was detected by AMU's distributed temperature system (DTS), suggesting the fracture occurred at 5:23 UTC. The distributed acoustic system (DAS) within AMU also supports this breakthrough, as the fibers strung throughout the AMU well, experience strain within an ~ 18 -hour window that encompassed the DTS anomaly. Therefore, we analyzed the source and receivers with a systematic approach to see if the receivers situated in the AMU well observed the breakthrough.

As observed in **Figure 3**, there is a shift early in the day of April 12th suggesting that the breakthrough was observed by receiver 16 which is situated in the AMU well. These features are shared with other receivers in the AMU well and lower alcove monitoring well (AML). Thus, we can observe the preconditions of the rock and potentially monitor the relaxation or altered condition of the fractured rock.

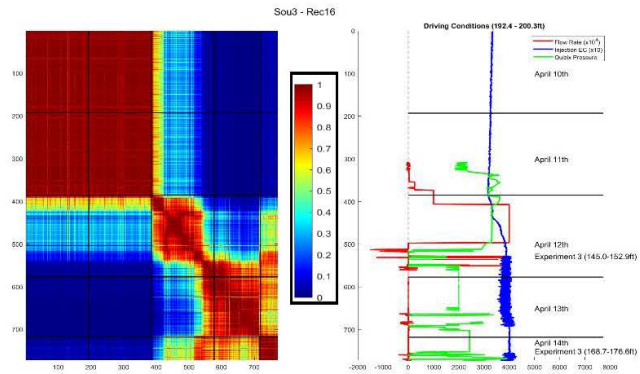


Figure 3. An example of a similarity matrix (left) for source 3 to receiver 16 for April 10th to April 12th. The testing conditions are plotted (right).

Therefore, the evolving conditions of the crystalline rock as suggested by DAS and DTS observations are reflected within the CASSM data as features within the similarity matrices of the source and receivers. Therefore, this analysis demonstrates that the coda signal is rich in information on the evolving condition of fractured rock and suggests the potential for remote monitoring of subsurface geothermal fracture systems.

Acknowledgments: This research was supported by CUSSP (Center for Understanding Subsurface Signals and Permeability), an Energy Earthshot Research Center funded by the U.S. Department of Energy (DOE), Office of Science under FWP 81834, and the National Science Foundation (NSF) REU grant PHY-2244297.

During constant rate-increasing injections on 12 April 2022, a fracture was induced that was situated in the upper monitoring alcove (AMU), where a subsequent shut-in test was executed. Essentially, the shut-in test allows for the pressure to decline, and the rock condition evolves.

Examining Acoustic Wave Interactions with Fracture Intersections

Erin Duell^{1,2}, Laura Pyrak-Nolte²

¹ The Ohio State University, ²Purdue University

The Enhanced Geothermal Systems (EGS) Collab Project aimed to stimulate fractures in a subsurface mine to explore the ability to enhance and control fracture network permeability to improve the commercial viability of geothermal energy sources. Experiment 2 of the EGS Collab project monitored, geophysically, the shear stimulation of intersecting fractures at the 4100 foot level at the Sanford Underground Research Facility (SURF) in Lead, South Dakota. Inspired by Experiment 2, the objective of this project is to replicate wave propagation across intersecting fractures in a laboratory setting to studying the compressional wave interaction with a fracture network and the resulting coda waves, i.e., late arriving composed of multiple internal reflections. From examination of the Collab field data interpretation, the intersection angles between the fractures varies along the intersection from 48 - 87 degrees.

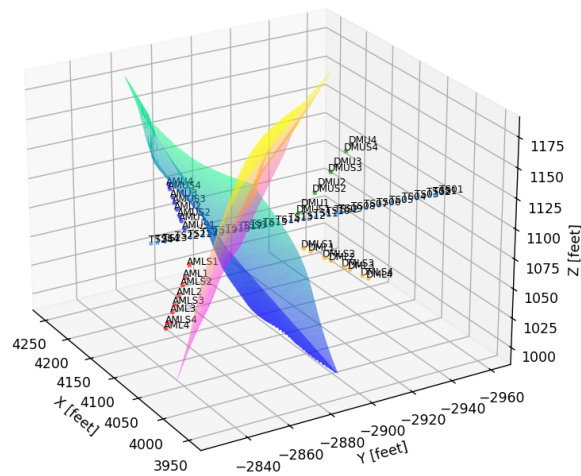


Figure 1: Visualization of the intersecting fractures plotted in Python

The objective of this study is to determine how the generation and signatures of coda waves are affected by the intersection angle and the fracture intersection. The fracture system geometry is mimicked using acrylic sheets in water to create an impedance contrast that would give rise to multiple reflections. The impedance contrast differs from that of the natural setting at SURF (i.e. fractures in amphibolite) where the impedance of the fracture region would be lower than the rock matrix. Obvious differences such as liquids not supporting shear

waves and different reflection angles will remove some components from the signals, but the goal here is to study coda wave generation from intersecting planes and intersections. However, this synthetic fracture network is a potential analog for mineral-filled fractures where the mineral seismic impedance is greater than the rock matrix. In the experimental set-up, a water-coupled piezoelectric source transducer is placed at a fixed location (opposite or offset from the intersection) while the receiving transducer is translated to record coda waves at various locations. Preliminary datasets were collected for different angles and geometries.

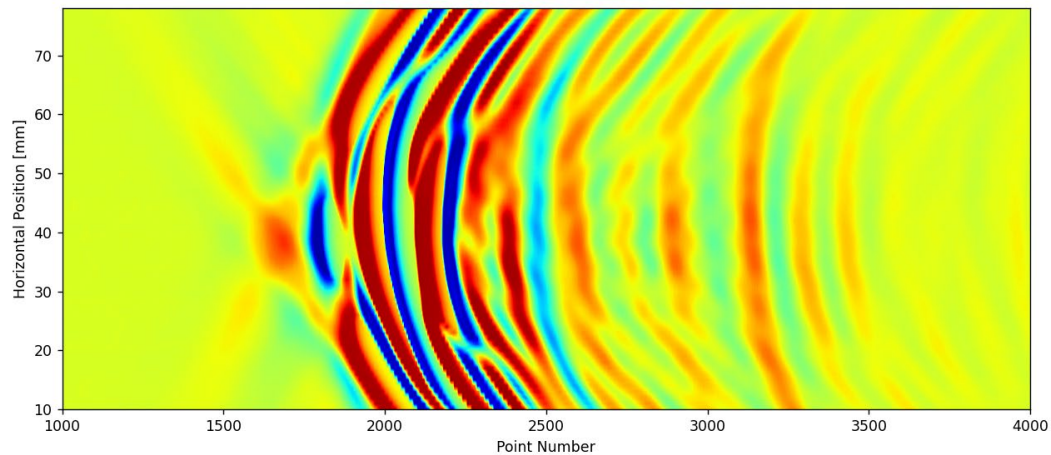


Figure 2: Waveform of 2 acrylic sheets placed in a V shape at a 90-degree angle. Note the 'X' shape before the first arrival

Analysis of the waveforms from the initial data set is underway, with attempts to understand and recreate the initial layout that caused the 'X' shape arrival before the first arrival (energy between 1500 – 1700 point numbers in Figure 2). Testing with geometries that better mimic the real fractures and with nylon sheets are ideal for next steps afterwards. I would like to thank Professor Pyrak-Nolte for her mentorship during this summer, and graduate student Alex Clark for all her help. This work was supported by the U.S. Department of Energy, Office of Science, Office of Basic Energy Sciences, Geosciences Research Program under Award Number (DE-SC0001048), and by NSF REU Grant Number (PHY-2244297).

Shearing Fracture Networks

Reagan Thompson^{1,2}, Laura Pyrak-Nolte²

¹ Tulsa Community College, ²Purdue University

Understanding the response of fracture networks under shear stress is crucial for applications concerning subsurface fluid flow where shear stimulation is often used to enhance fluid permeability. This study presents a laboratory method for examining the response of various pre-existing fracture topologies to vertical shearing while under constant horizontal confinement. 3D printed PMMA samples are subjected to controlled shearing with a Deben CT5000 in-situ uniaxial stress rig during X-ray microscopy (Zeiss Versa 510). 3D tomographic reconstructions are used to quantify and visualize the changes in fracture apertures as a function of loading. Data collected by these experiments will serve as a reference in the ongoing development of computational models of fracture dynamics and deformation. The combined result of this work will enable improved designs and efficiency in hydraulic fracturing systems through the optimization of shearing to enhance fluid flow.

Sample Preparation

Confinement is applied with polyethylene fishing line via a weight & pulley method that provides a constant tension in the line. This method was chosen due to its simple reproducibility and for its lack of obstruction during x-ray scanning. Stress relaxation, as seen in [3], was mitigated through knotting and allowing the sample a period to relax before use in experiment.

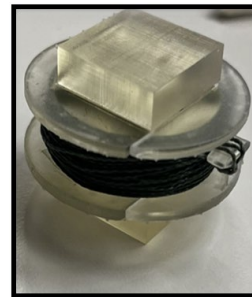


Figure 1: An example of a sample used in experiment.

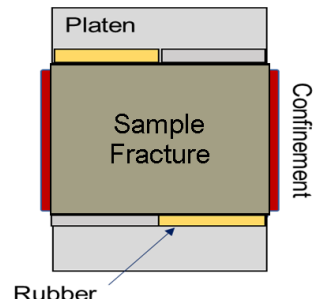
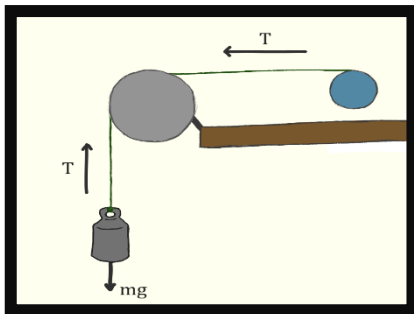


Figure 2: Diagram of typical sample anatomy.



Force measurements taken with an A201 Flexiforce sensor show consistent confinement pressure over many trials. Measurements taken were within the acceptable range of error given by [2]. 0.6 MPa confinement was used during experiment.

$$Pressure \propto \frac{tension * (no. of turns)}{radius * height}$$

Figure 3: A diagram demonstrating how samples were wrapped using a weight & pulley.

Roughness patterns were generated along fracture surfaces through a stratified percolation method presented in [1]. Roughness allows for a proper simulation of subsurface rock mechanics.

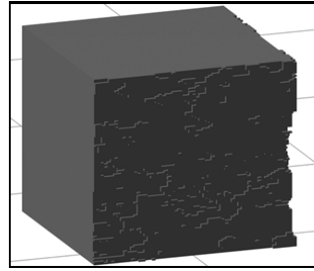


Figure 4: A simulated sample element with roughness.

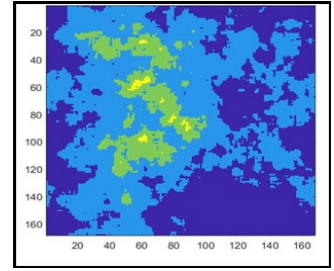


Figure 5: A roughness pattern generated by the method in [1]. Colors correspond to different heights.

Compression & X-Ray Microscopy

Samples undergo progressive vertical loading in the Deben, with 2D images captured during loading using the Zeiss for continuous analysis. Full tomographic scans at specific loads (250 N, 1000 N, and 2000 N) provide 3D reconstructions of the fracture network. This allows for the study of fracture aperture as compared to load, as well as the effects of other mechanical phenomena such as stress relaxation.



Figure 6: The Deben pictured inside of the Zeiss 3DXRM.

Scan Parameters:			
80 kV	7 Watts	Exposure: 3	Binning: 2
Pixel Resolution: 25.97 μ m			
Source Position: -90 mm		Detector Position: 148 mm	

Results

From X-ray imaging, the lateral confinement on the networks was sufficient to prevent significant shearing. Vertical fractures subjected to shearing were seen to open, while horizontal fractures closed under the normal loading. The torque observed on the “Slant” and “T” networks is attributed to the placement of the rubber.

Future efforts will seek to refine the presented methods, study fracture deformation under various confinement stresses and quantify shear stress through digital image correlation. This work will provide insight on how to optimize shear stimulation of fracture networks to enhance energy production.

References & Acknowledgements

- [1] Nolte, D. D., Pyrak-Nolte, L. J. (1991) Stratified continuum percolation: Scaling geometry of hierarchical cascades. *Physical Review A*, 44 (10). 6320-6333
doi:10.1103/physreva.44.6320
- [2] Swanson EC, Weathersby EJ, Cagle JC, Sanders JE. Evaluation of Force Sensing Resistors for the Measurement of Interface Pressures in Lower Limb Prosthetics. *J Biomech Eng*. 2019 Oct 1;141(10):1010091–10100913. doi: 10.1115/1.4043561. PMID: 31017621; PMCID: PMC6808001.
- [3] Cross, Rod & Lindsey, Crawford & Andruczyk, Daniel. (2000). Laboratory testing of tennis strings. *Sports Engineering*. 3. 219 - 230. 10.1046/j.1460-2687.2000.00064.x.

The laboratory data is based upon work supported by the U.S. Department of Energy, Office of Science, Office of Basic Energy Sciences, Geosciences Research Program under Award Number (DE-SC0001048). This work was supported by NSF REU grant PHY-2244297.

Many thanks go to Dr. Pyrak-Nolte for her guidance during this project and her role as an advisor.